

On-chip generation of hybrid polarization-frequency entangled biphoton states

S. FRANCESCONI,¹  A. RAYMOND,¹ R. DUHAMEL,¹ P. FILLoux,¹ A. LEMAÎTRE,²  P. MILMAN,¹ M. I. AMANTI,¹ F. BABOUX,^{1,*}  AND S. DUCCI¹ 

¹Université Paris Cité, CNRS, Laboratoire Matériaux et Phénomènes Quantiques, 75013 Paris, France

²Université Paris-Saclay, CNRS, Centre de Nanosciences et de Nanotechnologies, 91120 Palaiseau, France

*Corresponding author: florent.baboux@u-paris.fr

Received 13 April 2022; revised 10 November 2022; accepted 5 December 2022; posted 6 December 2022 (Doc. ID 459879); published 1 February 2023

We demonstrate a chip-integrated semiconductor source that combines polarization and frequency entanglement, allowing the generation of entangled biphoton states in a hybrid degree of freedom without post-manipulation. Our AlGaAs device is based on type-II spontaneous parametric downconversion in a counterpropagating phase-matching scheme in which the modal birefringence lifts the degeneracy between the two possible nonlinear interactions. This allows the direct generation of polarization–frequency entangled photons at room temperature and telecom wavelength, and in two distinct spatial modes, offering enhanced flexibility for quantum information protocols. The state entanglement is quantified by a combined measurement of the joint spectrum and Hong–Ou–Mandel interference (raw visibility $70.1\% \pm 1.1\%$) of the biphotons, allowing to reconstruct a restricted density matrix in the hybrid polarization–frequency space. © 2023 Chinese Laser Press

<https://doi.org/10.1364/PRJ.459879>

1. INTRODUCTION

Quantum states of light are central resources for quantum information technologies. Indeed, besides their easy transmission and robustness to decoherence, photons provide a large variety of degrees of freedom (DOFs) to encode information, which can be either two-dimensional (such as polarization) or higher-dimensional (such as frequency, orbital angular momentum, or spatial modes) [1,2]. In addition, photonic information can be encoded either in individual photons or in the quadratures of the electromagnetic field, defining, respectively, the realms of discrete variable (DV) and continuous variable (CV) encoding.

Polarization is a paradigmatic two-dimensional photonic DOF that allowed for pioneering demonstrations in quantum information, ranging from fundamental tests of quantum mechanics [3] to quantum computing [4] and communication tasks [5,6]. Focusing on DV encoding, polarization Bell states, such as $|\Psi^+\rangle_{\text{polar}} = (|H\rangle|V\rangle + |V\rangle|H\rangle)/\sqrt{2}$, where H and V stand for the horizontal and vertical polarizations of single photons, respectively, constitute a fundamental building block for many of these applications. They can be efficiently generated with parametric processes in nonlinear bulk crystals combined with external components (such as a walk-off compensator or a Sagnac interferometer) [7–10]. More recently, chip-based sources based on quantum dots [11–15] or parametric processes [16–20] allowed to generate polarization

Bell states in a fully integrated manner, without requiring external optical elements.

Now turning to high-dimensional photonic DOFs, among the various candidates, frequency is attracting growing interest due to its robustness to propagation in optical fibers and its capability to convey large-scale quantum information into a single spatial mode. Frequency is intrinsically a continuous DOF that can be used to encode information as such [21–23], but it can also be viewed as a discrete DOF when divided into frequency bins [24,25]. In the latter case, the simplest maximally entangled state of two photons is the so-called two-color Bell state, $|\Psi^+\rangle_{\text{col}} = (|\omega_1\rangle|\omega_2\rangle + |\omega_2\rangle|\omega_1\rangle)/\sqrt{2}$, where $|\omega_1\rangle$ and $|\omega_2\rangle$ are well-separated single-photon frequency bins. Several experimental schemes have been implemented to generate such two-color entangled states, which could be exploited, e.g., as a metrology resource for precise time measurements [26], or to interconnect stationary qubits with dissimilar energy levels [27] in a quantum network. The first realizations relied on filtering out frequency bins from a continuous spectrum [28,29]. More recently, brighter sources have been demonstrated by using periodically poled crystals in crossed configurations [26,30], Sagnac loops [31], double passage configurations [32], or by transferring entanglement from the polarization to the frequency domain [33]. All these demonstrations relied on bulk nonlinear crystals, and while integrated sources such as microring resonators are powerful to

generate frequency combs (involving a high number of frequency bins) [25], the direct and versatile generation of two-color entangled states with chip-based sources is still scarce. In the latter domain, an important advance was achieved in Ref. [34], combining on the same silicon chip two four-wave mixing sources and an interferometer with a reconfigurable phase shifter. The resulting interference between two independent sources allowed generating two-color entangled states in an integrated and controlled manner, albeit with limited efficiency.

Besides entanglement into a single DOF, combining several DOFs can provide increased flexibility for quantum information protocols. To this aim, we demonstrate here a single chip-integrated semiconductor source that combines frequency and polarization entanglement, leading to the generation of hybrid polarization–frequency entangled biphoton states without post-manipulation. Our AlGaAs device is based on type-II spontaneous parametric downconversion (SPDC) in a counter-propagating phase-matching scheme, where the modal birefringence lifts the spectral degeneracy between the two possible nonlinear interactions occurring in the device. This allows the direct generation of polarization–frequency entangled photons in two distinct spatial modes, at room temperature and telecom wavelength. Such combination of DOFs opens greater capabilities for quantum information applications, allowing to switch from one DOF to another and thus to adapt to different experimental conditions in a versatile manner.

2. THEORETICAL FRAMEWORK

Our semiconductor integrated source of photons pairs is sketched in Fig. 1(a). It is a Bragg ridge microcavity made of a stack of AlGaAs layers with alternating aluminum concentrations [19,35,36]. The source is based on a transverse pump scheme, where a pulsed laser beam impinging on top of the waveguide (with incidence angle θ with respect to the x axis) generates pairs of counterpropagating photons (signal and idler) through SPDC [19,37]. As a consequence of the opposite propagation directions for the photons, two type-II SPDC processes occur simultaneously in the device [19]: one that

generates a TE-polarized signal photon [propagating along $z > 0$; see Fig. 1(a)] and a TM-polarized idler photon (propagating along $z < 0$), and a second one that generates a TM-polarized signal and a TE-polarized idler. We later refer to these two generation processes as HV and VH , respectively, using the shorter notation H (horizontal) for TE and V (vertical) for TM. The central frequencies ω_s and ω_i of the signal and idler photons obey energy conservation ($\omega_p = \omega_s + \omega_i$, where ω_p is the pump frequency) and momentum conservation along the waveguide direction, which reads for the two interactions

$$\omega_p \sin(\theta) = \omega_s n_H(\omega_s) - \omega_i n_V(\omega_i) \quad [\text{Inter. } HV], \quad (1)$$

$$\omega_p \sin(\theta) = \omega_i n_V(\omega_i) - \omega_s n_H(\omega_s) \quad [\text{Inter. } VH], \quad (2)$$

with n_H and n_V the modal refractive indices of the waveguide for H and V polarizations, respectively.

Figure 1(b) shows the resulting SPDC tunability curve, i.e., the calculated central wavelengths of signal and idler photons as a function of the pump incidence angle θ , for both interactions, by taking into account our sample properties and the used pump central wavelength $\lambda_p = 773.15$ nm. The two interactions are not degenerate because of the small modal birefringence of the waveguide ($\Delta n = n_H - n_V \simeq 1.2 \times 10^{-2}$ at the working temperature 293 K). In the low-pumping regime, the generated two-photon state resulting from both interactions reads

$$|\Psi\rangle = \iint d\omega d\omega' [\phi_{HV}(\omega, \omega') \hat{a}_{s,H}^\dagger(\omega) \hat{a}_{i,V}^\dagger(\omega') + \phi_{VH}(\omega, \omega') \hat{a}_{s,V}^\dagger(\omega) \hat{a}_{i,H}^\dagger(\omega')] |0,0\rangle, \quad (3)$$

where the operator $\hat{a}_{s(i),H(V)}^\dagger(\omega)$ creates a signal (idler) photon of frequency ω and polarization H (V). The function $\phi_{HV}(\omega, \omega')$ is the joint spectral amplitude (JSA) for the interaction HV , i.e., the probability amplitude to measure an H signal photon at frequency ω and a V idler photon at frequency ω' ; the analogous definition goes for ϕ_{VH} .

To produce polarization–frequency entangled states, we consider the situation where the pump beam impinges at normal incidence on the waveguide ($\theta = 0^\circ$). The two interactions

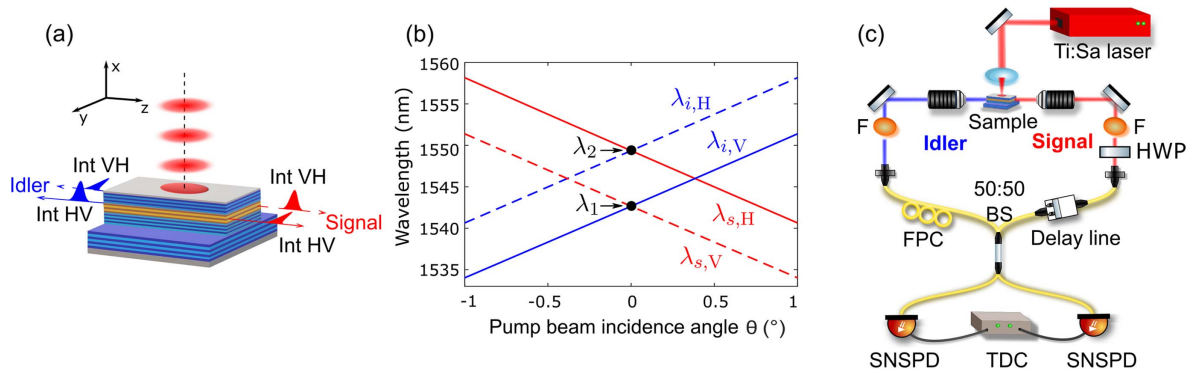


Fig. 1. (a) Schematic of an AlGaAs ridge microcavity emitting counterpropagating twin photons by SPDC in a transverse pump geometry. Two type-II interactions occur, generating either an H -polarized signal photon and a V -polarized idler photon (interaction HV), or the opposite situation (interaction VH), resulting in a hybrid polarization–frequency entangled state. (b) Calculated SPDC tunability curve, showing the central wavelengths of signal and idler photons as a function of the pump incidence angle θ (with respect to the vertical x axis), for both interactions, using our sample properties and pump central wavelength $\lambda_p = 773.15$ nm. (c) Sketch of the experimental setup to measure the HOM interference of the hybrid polarization–frequency state. HWP, half-wave plate; F, frequency filter; FPC, fibered polarization controller; BS, beam splitter; SNSPD, superconducting nanowire single-photon detector; TDC, time-to-digital converter.

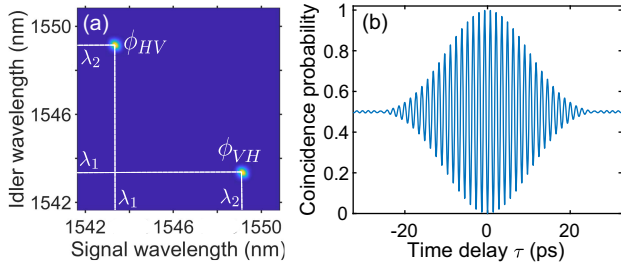


Fig. 2. (a) Simulated joint spectral intensity (JSI) of the hybrid polarization–frequency biphoton state of Eq. (3), assuming Gaussian phase-matching functions (see text for details). (b) Corresponding simulated HOM interferogram, showing a sinusoidal oscillation modulated by a Gaussian envelope.

give rise to two distinct peaks in the biphoton spectrum, as seen in the simulation of Fig. 2(a) showing the joint spectral intensity (JSI), which is the modulus squared of the JSA (plotted in the wavelength space). The two peaks, centered at wavelengths λ_1 and λ_2 [see Fig. 1(b)], are symmetric with respect to the degeneracy wavelength $\lambda_{\text{deg}} = 2\lambda_p$. Since the separation between the peaks is much larger than their spectral widths, a reasonable approximation is to discretize the frequency DOF and replace the JSAs by Dirac deltas, $\phi_{HV}(\omega, \omega') = \phi_{VH}(\omega', \omega) = \delta(\omega - \omega_1, \omega' - \omega_2)$ (with $\omega_{1(2)} = 2\pi c/\lambda_{1(2)}$). Inserting these expressions into Eq. (3), the emitted biphoton state can be rewritten as a hybrid polarization–frequency (HPF) state, $|\Psi\rangle \simeq |\Psi\rangle_{\text{HPF}}$, with

$$|\Psi\rangle_{\text{HPF}} = \frac{1}{\sqrt{2}} (|H\omega_1\rangle_s |V\omega_2\rangle_i + |V\omega_2\rangle_s |H\omega_1\rangle_i). \quad (4)$$

The first ket represents the signal photon and the second the idler photon, as defined by their respective opposite propagation directions. In this state, frequency ω_1 is always associated with H polarization, while frequency ω_2 is always associated with V polarization. This constitutes a composite polarization–frequency DOF, and state Eq. (4) is maximally entangled in this composite DOF. An advantage of such a kind of entangled states is its versatility, since upon manipulation with simple optical elements, the state of Eq. (4) can be projected on either a polarization Bell state [38] or a two-color Bell state [33], so as to adapt to a specific experimental context.

To reveal and quantify the entanglement level of the HPF state, two-photon interference in a Hong–Ou–Mandel (HOM) experiment provides a powerful tool, as it directly probes the quantum coherence between the two components of the state. When the signal and idler photons are delayed by a time τ and sent into the two input ports of a balanced beam splitter, the coincidence probability between the beam splitter outputs can be calculated from the JSAs ϕ_{HV} and ϕ_{VH} of the two SPDC processes:

$$P_c(\tau) = \frac{1}{2} - \text{Re} \left[\iint d\omega d\omega' \phi_{HV}(\omega, \omega') \phi_{VH}^*(\omega', \omega) e^{-i(\omega - \omega')\tau} \right], \quad (5)$$

where “Re” denotes the real part. Coming back to the continuous (rather than Dirac delta) expression of the joint spectra, and considering a narrow pump bandwidth and negligible group

velocity dispersion (as justified in our experimental conditions), the JSAs can be written as $\phi_a(\omega, \omega') = \phi_a^{\text{spec}}(\omega_+) \phi_a^{\text{pm}}(\omega_-)$ (with $a = HV$ or VH), where we have introduced $\omega_{\pm} = \omega \pm \omega'$ [39,40]. The function ϕ_a^{spec} , corresponding to the condition of energy conservation, is given by the spectrum of the pump beam, while the function ϕ_a^{pm} , reflecting the phase-matching condition, is determined by the spatial properties of the pump beam [19,39]. Due to the separability of the JSAs in ω_+ and ω_- , the HOM coincidence probability is actually determined only by the phase-matching part of the JSAs [40,41]. Considering a Gaussian pump spot of waist w_z along the waveguide direction, the phase-matching functions of the two interactions can be calculated as

$$\begin{aligned} \phi_{HV}^{\text{pm}}(\omega_-) &= \sqrt{\pi} w_z e^{-(\omega_- - \mu)^2 / 2\Delta\omega_-^2}, \\ \phi_{VH}^{\text{pm}}(\omega_-) &= \sqrt{\pi} w_z e^{-(\omega_- + \mu)^2 / 2\Delta\omega_-^2}, \end{aligned} \quad (6)$$

where $\Delta\omega_- = \sqrt{2}v_g/w_z$ is the spectral width of each interaction and $\mu = \omega_1 - \omega_2 = v_g\omega_p(n_H - n_V)/2c$ their spectral separation, with v_g the harmonic mean of the group velocities of the SPDC modes [39]. Inserting Eq. (6) into the expression of the coincidence probability Eq. (5) leads to

$$P_c(\tau) = \frac{1}{2} - \frac{1}{2} \exp\left(-\frac{\tau^2}{2\Delta\tau^2}\right) \cos(\mu\tau). \quad (7)$$

The resulting interferogram, plotted in Fig. 2(b), displays a sinusoidal oscillation (spatial quantum beating), of frequency μ equal to the spectral separation of the frequency modes, and modulated by a Gaussian envelope of width $\Delta\tau = \sqrt{2}/\Delta\omega_-$ determined by the spectral width of each interaction.

3. EXPERIMENTS

The epitaxial structure of the sample is made of a 4.5-period $\text{Al}_{0.80}\text{Ga}_{0.20}\text{As}/\text{Al}_{0.25}\text{Ga}_{0.75}\text{As}$ core, surrounded by two distributed Bragg mirrors made of a 36- and 14-period $\text{Al}_{0.90}\text{Ga}_{0.10}\text{As}/\text{Al}_{0.35}\text{Ga}_{0.65}\text{As}$ stacks for bottom and top mirrors, respectively. The Bragg mirrors provide both a vertical microcavity to enhance the pump field and a cladding for the twin-photon modes. From this planar structure, a ridge waveguide (length 2.6 mm, width 5 μm , and height 7 μm) is fabricated by UV photolithography followed by wet etching (see Appendix A for more details). The waveguide facets are then coated with a thin SiO_2 film (target thickness 270 nm) deposited by plasma-enhanced chemical vapor deposition (PECVD), resulting in a $\simeq 10\%$ modal reflectivity for the SPDC modes.

The experimental setup is shown in Fig. 1(c). The sample is pumped with a pulsed Ti:Sa laser of central wavelength $\lambda_p \simeq 773.15$ nm, pulse duration 4.5 ps, repetition rate 76 MHz, and average power 30 mW on the sample. A cylindrical lens focuses the pump beam into a Gaussian elliptical spot on top of the waveguide (waist $w_z = 1$ mm along the waveguide direction) at perpendicular incidence ($\theta = 0^\circ$), and the generated infrared photons are collected with two microscope objectives and collimated into single-mode optical fibers (with a total chip-to-fiber coupling efficiency $\sim 20\%$). The measured propagation losses are of 0.6 ± 0.1 cm^{-1} for both TE and TM fundamental modes of the waveguide. The sample temperature is stabilized at 293 K using a Peltier controller.

We first characterize the generated quantum state by measuring the JSI using a fiber spectrograph [42]. For this, the signal

and idler photons are separately sent into a spool of highly dispersive fiber, converting the frequency information into time-of-arrival information. The latter is recorded using superconducting nanowire single-photon detectors (SNSPDs, of detection efficiency 90%) connected to a time-to-digital converter (TDC); long-pass filters are used to remove slight luminescence noise from the sample. The measured JSI, reported in Fig. 3(a), shows two well-defined frequency peaks, symmetric with respect to the degeneracy wavelength, in good qualitative agreement with the numerical simulation of Fig. 2(a). This can be better seen in Fig. 3(b), showing the marginal spectrum of signal (red) and idler (blue) photons as extracted from the experimental JSI. The frequency peaks have an FWHM of ≈ 0.5 nm and separation $\Delta\lambda = \lambda_2 - \lambda_1 \approx 4.8$ nm, i.e., about 10 times higher than their linewidths. The measured $\Delta\lambda$ is smaller than in the simulation [6.2 nm in Fig. 2(a)], pointing to a discrepancy between the experimental and simulated modal birefringence $\Delta n = n_H - n_V$. This could be due to a slight deviation of the epitaxial structure from the nominal one and/or imperfections of the simulation (used material refractive indices and exact etching shape of the waveguide); for large waveguides as considered here, numerical simulations show that the epitaxial structure (slight uncertainty in the aluminum concentration and height of the layers) is the dominant factor.

We now perform two-photon interference in an HOM setup [see Fig. 1(c)] to reveal the entanglement properties of the generated HPF state. A half-wave plate (HWP) in the signal arm and a fibered polarization controller (FPC) in the idler arm are used to compensate for polarization rotation on the optical path, hence maintaining signal and idler photons in the same state as at the chip output so that they enter the beam splitter with crossed polarizations. The resulting interferogram, shown in Fig. 3(c) (black points with error bars), displays a clear sinusoidal modulation with a Gaussian envelope. Each point is obtained by a 20 s integration time, and error bars are calculated assuming a Poissonian statistics. The data are fitted (blue line) using a modified version of Eq. (7) accounting for experimental imperfections:

$$P_c(\tau) = \frac{1}{2} \left[1 - V \exp\left(-\frac{\tau^2}{2\Delta\tau^2}\right) \cos(\mu\tau) \right] + a\tau + b, \quad (8)$$

where V is the interferogram visibility, and the linear term $a\tau + b$ accounts for a slight drift of the alignment during

the total time of the measurement. The fitted envelope width is $\Delta\tau = 10.0$ ps, in good agreement with the simulation (10.5 ps) of Fig. 2(b). The fitted oscillation period is $2\pi/\mu = 1.8$ ps, in good agreement with the spectral measurement of the peak separation μ [Fig. 3(b)], but higher than in the simulation (1.3 ps), for the same reasons as mentioned above.

The experimental raw visibility is $V = 70.1\% \pm 1.1\%$. We attribute the main part of the visibility reduction to the non-zero reflectivity of the facets. Indeed, as a consequence of the latter, the two photons of each pair have a non-zero probability to exit through the same facet, instead of opposite ones. This results in quantum interference between the situation where both photons exit from one facet and the situation where both photons exit from the other facet, leading to a modulation at a frequency equal to the sum of signal and idler frequencies, i.e., the pump frequency ω_p . This interference occurs for a time delay shorter than the temporal width of the SPDC photons, and therefore, it is superimposed to the HOM interference [43]. The corresponding period is $2\pi/\omega_p \approx 2$ fs, which is beyond the resolution of our HOM setup. The measured interferogram thus averages out over these rapid oscillations, reducing the effective visibility of the fringes. For our sample with 10% reflectivity for SPDC modes, numerical simulations including this averaging effect predict a visibility of 82% (see Appendix A). We attribute the remaining visibility drop to slight imperfections of the pump spatial profile and incidence angle (see Appendix A for a detailed discussion on this effect and on other possible causes of visibility reduction in the experiment).

Using the joint spectrum and HOM measurements, we can now quantify the entanglement of the generated HPF state by estimating a restricted density matrix [33] in the polarization-frequency discrete space. The full basis would include all combinations of the $\{H, V\}$ polarizations and $\{\omega_1, \omega_2\}$ frequencies, resulting in a 16×16 density matrix. However, physical considerations allow for restricting the relevant basis dimension, projecting it onto the relevant subspace. Indeed, the employed type-II SPDC process does not allow the production of photons of the same polarization, while energy conservation forbids the production of photons of the same frequency; in addition, the phase matching requires that photons of frequency ω_1 (resp. ω_2) are always V (resp. H) polarized. This leads to the following 4×4 restricted density matrix:

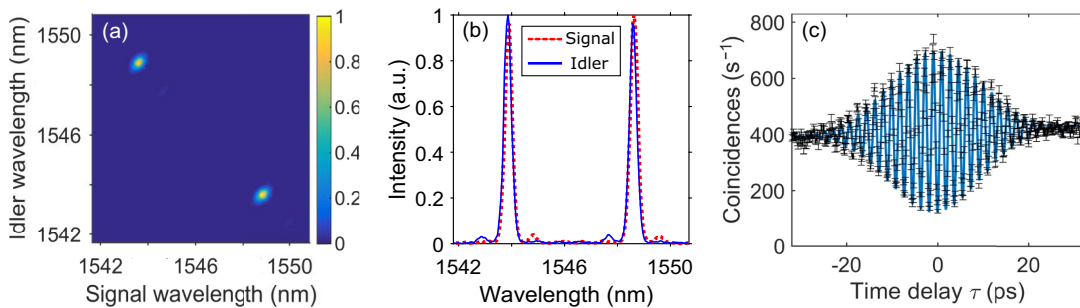


Fig. 3. (a) Measured joint spectral intensity (JSI) of the hybrid polarization–frequency state, and (b) corresponding marginal spectrum of signal (red line) and idler (blue line) photons. (c) Measured HOM interferogram (black symbols with error bars) fitted with Eq. (8) (blue line). Data points show raw (uncorrected) coincidence counts.

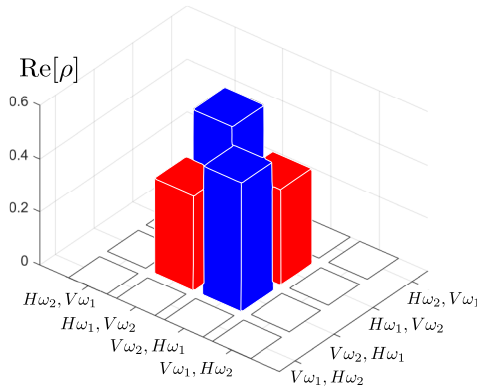


Fig. 4. Experimental reconstruction of the restricted density matrix [Eq. (9)] of the biphoton state in the hybrid polarization–frequency discrete space (the imaginary part is zero by construction).

$$\rho = \begin{pmatrix} 0 & 0 & 0 & 0 \\ 0 & p & \frac{V}{2}e^{i\phi} & 0 \\ 0 & \frac{V}{2}e^{-i\phi} & 1-p & 0 \\ 0 & 0 & 0 & 0 \end{pmatrix}, \quad (9)$$

expressed in the basis $\{|H\omega_2\rangle_s|V\omega_1\rangle_i, |H\omega_1\rangle_s|V\omega_2\rangle_i, |V\omega_2\rangle_s|H\omega_1\rangle_i, |V\omega_1\rangle_s|H\omega_2\rangle_i\}$. Parameters p (balance parameter) and V (visibility) are real and obey the physical constraints $0 \leq p \leq 1$ and $0 \leq V/2 \leq \sqrt{p(1-p)}$ [33].

The JSI measurement [Fig. 3(a)] yields the population term $p = 0.517 \pm 0.005$ (obtained by integrating coincidence counts in a square window of 2 nm width centered on each of the two spectral modes) while the HOM interferogram [Fig. 3(c)] gives the coherence modulus $V/2$ from the visibility deduced above; the phase $\phi = 0$ between the two interactions is deduced from the fact that the source is pumped by a single pump beam. The resulting density matrix is shown in Fig. 4. It allows to extract the purity of the generated state, $P = 0.746 \pm 0.008$, its fidelity to the ideal state of Eq. (4), $F = 0.851 \pm 0.007$, and its concurrence, $C = 0.701 \pm 0.011$ (all raw values). This confirms the direct generation of HPF entanglement by our chip-integrated source. The generation rate, estimated from single and coincidence counts data [44], is $\approx 10^7$ pairs/s at the chip output for the used pump power $P = 30$ mW incident on the sample.

4. DISCUSSION AND CONCLUSION

In summary, we have demonstrated a chip-based semiconductor source that combines polarization and frequency entanglement, enabling the generation of HPF entangled photon pairs directly at the generation stage, in two distinct spatial modes. Such combination of DOFs provides an increased flexibility for quantum information protocols, allowing to adapt the source to different applications in a versatile manner. The demonstrated device operates at room temperature and telecom wavelength and has a strong potential for integration within photonic circuits [45–47]. Due to the direct bandgap of AlGaAs, it is also compliant with electrical pumping, either by monolithic integration with a laser diode [48] or through adhesive bonding

of a VCSEL with a large rectangular aperture, as demonstrated, e.g., in Ref. [49], on top of the structure.

These results could be further expanded along several directions. First, the fidelity of the experimentally generated state to the ideal HPF state of Eq. (4) could be improved by implementing a multi-layer coating of the waveguide facets, allowing to reach modal reflectivities $\leq 1\%$. This enhancement would lead to an expected fidelity larger than 0.93, all other factors (including experimental imperfections) kept unchanged. The fidelity could be further improved by correcting for the small imperfections of the pump spatial profile (deviations from the ideal Gaussian shape) using, e.g., a spatial light modulator.

In addition, the frequency entanglement of our HPF state can be varied by different means. In Eq. (4), frequency entanglement is described as a discrete two-color entanglement, which reflects the dominant frequency anticorrelation of the state, but neglects intra-mode frequency entanglement, i.e., the continuous entanglement associated with the internal structure of each frequency mode [as determined by JSAs ϕ_{HV} and ϕ_{VH} in Eq. (3)]. This intra-mode entanglement, which manifests in the envelope of HOM oscillations [Eq. (7)], can be controlled *in situ*. Indeed, a specific asset of our counter-propagating phase-matched source is that the JSA can be engineered through the spatial properties of the pump beam [39]. We have here implemented Gaussian JSAs [Eq. (6)], which leads to a Gaussian envelope in the HOM interferogram; the width of this envelope could be varied by changing the waist of the pump beam. Going beyond, more complex types of intra-mode entanglement could be designed by tailoring the spatial phase of the pump beam [50,51], leading to various envelope shapes that could be exploited, e.g., for quantum metrology based on HOM interferometry [26,52].

Frequency entanglement can also be tailored at the inter-mode level, i.e., by varying the separation between the two central frequencies (ω_1 and ω_2). This can be achieved by playing with the modal birefringence of the waveguide, either *in situ* by changing the working temperature, or at the fabrication step by varying the width of the waveguide. Numerical simulations show that the birefringence $\Delta n = n_H - n_V$ decreases as the waveguide width is decreased, reaching zero for a width of ≈ 1.3 μm . In the latter situation, the two interactions become spectrally degenerate, and the two frequency modes collapse. Thus, inter-mode frequency entanglement vanishes, but intra-mode entanglement, as determined by the JSA, remains and is decoupled from polarization entanglement. This would lead to a hyper-entangled polarization–frequency state, in the tensor product form $(|H\rangle_s|V\rangle_i + |V\rangle_s|H\rangle_i)/\sqrt{2} \otimes \iint d\omega d\omega' \phi(\omega, \omega') |\omega\rangle_s |\omega'\rangle_i$. This situation opens stimulating perspectives for the implementation of quantum information tasks [53–55], in particular, in the field of quantum communication to improve bit rates and resilience to noise [56–59].

APPENDIX A

1. Sample Fabrication

From the planar AlGaAs epitaxial structure described in the main text, ridge waveguides are patterned by photolithography followed by wet etching. We employed UV photolithography (MJB4 machine) with a positive photoresist S1805 (nominal

thickness of 500 nm) and a custom Cr photomask from Delta Mask. The resist is developed using an MF-319 developer, and the waveguides are then etched using a solution composed of acetic acid, potassium dichromate ($K_2Cr_2O_7$), and hydrobromic acid (HBr) in stoichiometric proportions. This wet etching technique yields curved sidewalls. The width value given in the paper (5 μm) corresponds to the width at the top of the waveguide, while the height value (7 μm) corresponds to the total height between the top and bottom (far from the waveguide) of the structure. These parameters can be measured either by SEM or a Dektak profilometer, yielding consistent results. As mentioned in the main text, for such relatively large waveguide widths, we verified by numerical simulations that the precise shape of the confinement has little effect on the modal birefringence, which is mainly determined by the epitaxial structure.

2. Calculation of HOM Interferogram with Fabry–Pérot Effect

We state in the paper that the non-zero reflectivity of the waveguide facets is the main source of limitation of visibility in the measured HOM interferogram of the HPF state [Fig. 3(c)]. We here demonstrate it by expanding our theoretical treatment to account for the Fabry–Pérot cavity effect induced by the facets.

We model the HOM experiment as shown in Fig. 5, where the letters define the subscripts used in the calculations that follow. The source generates signal and idler photons: s and i label the propagation directions of the generated photons inside the source before mixing by the Fabry–Pérot cavity (materialized by mirrors in the figure), while \mathcal{R} (right) and \mathcal{L} (left) denote the propagation directions outside the cavity. Ports 1 and 2 are the two inputs of the beam splitter, and 3 and 4 are the two outputs between which coincidences are measured. A delay line is placed in the \mathcal{R} path.

We start from the expression of the emitted state without cavity effect [Eq. (3)]. The reflection and transmission coefficients (in amplitude) of the cavity are written respectively as

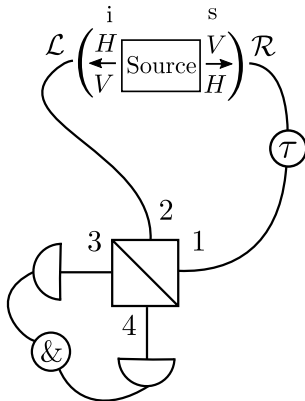


Fig. 5. Hong–Ou–Mandel scheme for a counterpropagating parametric source emitting photons through both HV and VH interactions and considering the cavity effect induced by the waveguide facets. The letters refer to the subscripts used in the calculations.

$$f_r(\omega) = \frac{\sqrt{R(1-R)} \exp\left(i \frac{3\omega nL}{2c}\right)}{1 - R \exp\left(i \frac{2\omega nL}{c}\right)},$$

$$f_t(\omega) = \frac{\sqrt{1-R} \exp\left(i \frac{\omega nL}{2c}\right)}{1 - R \exp\left(i \frac{2\omega nL}{c}\right)}, \quad (\text{A1})$$

where R is the modal reflectivity (in intensity) of the SPDC modes, n their modal refractive index, and L the waveguide length. We assume for simplicity that R and n are the same for both polarizations (which is correct within 5% for our sample). Each waveguide facet is then modeled as a frequency-dependent beam splitter [60], where photons can be either reflected or transmitted with a probability depending on their frequency. The corresponding transformations for the \hat{a} and \hat{a}^\dagger operators read

$$\hat{a}_{s,\sigma}^\dagger(\omega) \rightarrow f_t(\omega) \hat{a}_{\mathcal{R},\sigma}^\dagger(\omega) + f_r(\omega) \hat{a}_{\mathcal{L},\sigma}^\dagger(\omega),$$

$$\hat{a}_{i,\sigma}^\dagger(\omega) \rightarrow f_t(\omega) \hat{a}_{\mathcal{L},\sigma}^\dagger(\omega) + f_r(\omega) \hat{a}_{\mathcal{R},\sigma}^\dagger(\omega), \quad (\text{A2})$$

where σ stands for H or V polarization. Starting from Eq. (3), applying transformation Eq. (A2) and adding the effect of the delay line (delay τ) leads to the following expression for the biphoton state just before the beam splitter:

$$|\Psi\rangle = \iint d\omega_1 d\omega_2 \left\{ \phi_{HV}(\omega_1, \omega_2) [f_t(\omega_1) \hat{a}_{\mathcal{R},H}^\dagger(\omega_1) e^{-i\omega_1 \tau} + f_r(\omega_1) \hat{a}_{\mathcal{L},H}^\dagger(\omega_1)] \cdot [f_t(\omega_2) \hat{a}_{\mathcal{L},V}^\dagger(\omega_2) + f_r(\omega_2) \hat{a}_{\mathcal{R},V}^\dagger(\omega_2) e^{-i\omega_2 \tau}] + \phi_{VH}(\omega_1, \omega_2) [f_t(\omega_1) \hat{a}_{\mathcal{R},V}^\dagger(\omega_1) e^{-i\omega_1 \tau} + f_r(\omega_1) \hat{a}_{\mathcal{L},V}^\dagger(\omega_1)] \cdot [f_t(\omega_2) \hat{a}_{\mathcal{L},H}^\dagger(\omega_2) + f_r(\omega_2) \hat{a}_{\mathcal{R},H}^\dagger(\omega_2) e^{-i\omega_2 \tau}] \right\} |0,0\rangle. \quad (\text{A3})$$

We then apply the usual beam splitter transformations:

$$\hat{a}_1^\dagger(\omega) \rightarrow \frac{1}{\sqrt{2}} [\hat{a}_3^\dagger(\omega) + i \hat{a}_4^\dagger(\omega)],$$

$$\hat{a}_2^\dagger(\omega) \rightarrow \frac{1}{\sqrt{2}} [\hat{a}_4^\dagger(\omega) + i \hat{a}_3^\dagger(\omega)], \quad (\text{A4})$$

and since we are interested in coincidence events, only the crossed terms (of the kind $\hat{a}_3^\dagger \hat{a}_4^\dagger$ and $\hat{a}_4^\dagger \hat{a}_3^\dagger$) are considered. The resulting effective wave function $|\Psi_c\rangle$ reads

$$|\Psi_c\rangle = \frac{1}{2} \iint d\omega_1 d\omega_2 \left[A(\omega_1, \omega_2) \hat{a}_{3,H}^\dagger(\omega_1) \hat{a}_{4,V}^\dagger(\omega_2) + B(\omega_1, \omega_2) \hat{a}_{3,H}^\dagger(\omega_2) \hat{a}_{4,V}^\dagger(\omega_1) + C(\omega_1, \omega_2) \hat{a}_{3,V}^\dagger(\omega_1) \hat{a}_{4,H}^\dagger(\omega_2) + D(\omega_1, \omega_2) \hat{a}_{3,V}^\dagger(\omega_2) \hat{a}_{4,H}^\dagger(\omega_1) \right] |0,0\rangle, \quad (\text{A5})$$

where the coefficients are

$$A(\omega_1, \omega_2) = \phi_{HV}(\omega_1, \omega_2) [-f_r(\omega_1) f_r(\omega_2) e^{-i\omega_2 \tau} + i f_t(\omega_1) f_r(\omega_2) e^{-i(\omega_1 + \omega_2) \tau} + i f_r(\omega_1) f_t(\omega_2) + i f_t(\omega_1) f_t(\omega_2) e^{-i\omega_1 \tau}], \quad (\text{A6})$$

$$B(\omega_1, \omega_2) = \phi_{VH}(\omega_1, \omega_2) [f_r(\omega_1)f_r(\omega_2)e^{-i\omega_2\tau} + if_t(\omega_1)f_r(\omega_2)e^{-i(\omega_1+\omega_2)\tau} + if_r(\omega_1)f_t(\omega_2) - if_t(\omega_1)f_t(\omega_2)e^{-i\omega_1\tau}], \quad (\text{A7})$$

$$C(\omega_1, \omega_2) = \phi_{VH}(\omega_1, \omega_2) [-f_r(\omega_1)f_r(\omega_2)e^{-i\omega_2\tau} + if_t(\omega_1)f_r(\omega_2)e^{-i(\omega_1+\omega_2)\tau} + if_r(\omega_1)f_t(\omega_2) + if_t(\omega_1)f_t(\omega_2)e^{-i\omega_1\tau}], \quad (\text{A8})$$

$$D(\omega_1, \omega_2) = \phi_{HV}(\omega_1, \omega_2) [f_r(\omega_1)f_r(\omega_2)e^{-i\omega_2\tau} + if_t(\omega_1)f_r(\omega_2)e^{-i(\omega_1+\omega_2)\tau} + if_r(\omega_1)f_t(\omega_2) - if_t(\omega_1)f_t(\omega_2)e^{-i\omega_1\tau}]. \quad (\text{A9})$$

In general, the coincidence probability P_c would consist of four contributions corresponding to the detection of HH , VV , HV , or VH photons at the beam splitter output. However, even if the photons are mixed by the cavity, they are always generated with crossed polarizations so that the HH and VV events can be neglected. The coincidence probability for the HV and VH events can be calculated as the expectation value of coincidence operators \hat{M}_{HV} and \hat{M}_{VH} :

$$\begin{aligned} \hat{M}_{HV} &= \int d\omega_3 \hat{a}_{3,H}^\dagger(\omega_3) |0\rangle \langle 0| \hat{a}_{3,H}(\omega_3) \\ &\quad \cdot \int d\omega_4 \hat{a}_{4,V}^\dagger(\omega_4) |0\rangle \langle 0| \hat{a}_{4,V}(\omega_4), \\ \hat{M}_{VH} &= \int d\omega_3 \hat{a}_{3,V}^\dagger(\omega_3) |0\rangle \langle 0| \hat{a}_{3,V}(\omega_3) \\ &\quad \cdot \int d\omega_4 \hat{a}_{4,H}^\dagger(\omega_4) |0\rangle \langle 0| \hat{a}_{4,H}(\omega_4). \end{aligned} \quad (\text{A10})$$

The resulting coincidence probabilities read

$$\begin{aligned} P_{HV}(\tau) &= \langle \Psi_c | \hat{M}_{HV} | \Psi_c \rangle \\ &= \frac{1}{4} \iint d\omega_3 d\omega_4 [|A(\omega_3, \omega_4)|^2 \\ &\quad + |B(\omega_3, \omega_4)|^2 + A^*(\omega_3, \omega_4)B(\omega_4, \omega_3) \\ &\quad + A(\omega_4, \omega_3)B^*(\omega_3, \omega_4)], \end{aligned} \quad (\text{A11})$$

$$\begin{aligned} P_{VH}(\tau) &= \langle \Psi_c | \hat{M}_{VH} | \Psi_c \rangle \\ &= \frac{1}{4} \iint d\omega_3 d\omega_4 [|C(\omega_3, \omega_4)|^2 \\ &\quad + |D(\omega_3, \omega_4)|^2 + C^*(\omega_3, \omega_4)D(\omega_4, \omega_3) \\ &\quad + C(\omega_4, \omega_3)D^*(\omega_3, \omega_4)], \end{aligned} \quad (\text{A12})$$

which leads to the total coincidence probability $P_c(\tau) = P_{HV}(\tau) + P_{VH}(\tau)$.

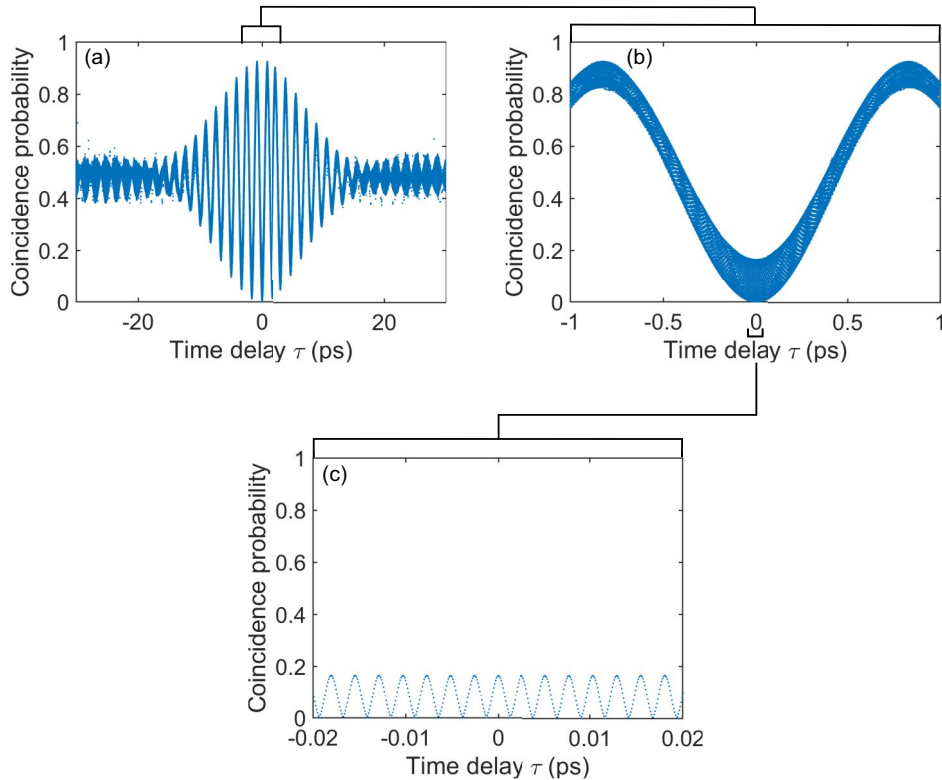


Fig. 6. Simulated HOM interferogram for the HPF entangled state, taking into account the Fabry–Pérot effect of the sample with facet reflectivity $R = 10\%$. From (a) to (c), the time axis is zoomed around $\tau = 0$ to show the additional modulation at the pump frequency. The scattered points are caused by numerical artifacts in the integration.

We numerically evaluate $P_c(\tau)$ by considering Gaussian phase-matching functions [Eq. (6)] with parameters given by the experiment and facet reflectivity $R = 0.1$. Figure 6 shows the calculated HOM interferogram for different levels of close-up around $\tau = 0$. The general shape of the coincidence probability [Fig. 6(a)] is similar to the case without cavity effect [Fig. 2(b)], with a Gaussian-like envelope and a sinusoidal oscillation. However, zooming in we note another oscillation superimposed to the first one [Figs. 6(b) and 6(c)]. This modulation has a period of 2.3 fs, corresponding to the inverse of the pump frequency ($2\pi/\omega_p$).

As stated in the main text, the used HOM experimental setup does not have enough resolution (i.e., mechanical and thermal stability of the mirrors and of the delay line) to resolve this oscillation at the pump frequency, and thus only its temporal average is measured. The latter is numerically evaluated in Fig. 7. We observe a reduction of the effective visibility of the fringes to $\approx 82\%$. As mentioned in Section 4, using a multi-layer instead of single-layer coating could decrease the facet reflectivities to $\leq 1\%$, for which the theoretical HOM visibility would be $\geq 98\%$ (all other conditions assumed to be perfect).

The experimentally measured visibility is $\approx 70\%$. We attribute the additional visibility drop (with respect to the above simulated 82%) to slight imperfections of the pump spatial profile and incidence angle, not considered in the simulation above. These pump imperfections, when considered alone, typically lead to a $\approx 10\%$ visibility reduction as we observed in Ref. [50] by carrying out the HOM experiment in a very similar sample, but in a simpler situation where only photons from a single nonlinear interaction were considered.

Other possible sources of visibility reduction could in principle be related to multi-pair emission or sample photoluminescence. The coincidence-to-accidental ratio (CAR) measured in the experiment is 42, where accidental coincidences are dominated by coincidences between an “orphan” photon (whose twin has been lost or undetected) and a noise count coming from photoluminescence, multi-pair emission (photon coming from another, uncorrelated pair), or detector dark count. The high measured CAR suggests that photoluminescence and multi-pair emission are maintained to a low level in the experiment, thus having a negligible impact on the HOM experiment. This is corroborated by the fact that no detectable increase of HOM visibility was observed when reducing the pump power in our experiments.

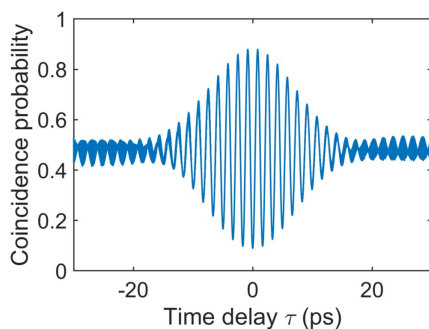


Fig. 7. Simulated HOM interferogram obtained from the data of Fig. 6 by averaging out modulation at the pump frequency, leading to a decrease of effective fringe visibility.

Acknowledgment. We acknowledge support from European Union’s Horizon 2020 research and innovation programme under the HORIZON EUROPE Marie Skłodowska-Curie Actions grant agreement No. 665850, Paris Ile-de-France Région in the framework of DIM SIRTEQ (LION project), Ville de Paris Emergence program (LATTICE project), IdEx Université Paris Cité (ANR-18-IDEX-0001), Labex SEAM (Science and Engineering for Advanced Materials and Devices, ANR-10-LABX-0096), and the French RENATECHnetwork.

Disclosures. The authors declare no conflicts of interest.

Data Availability. Data underlying the results presented in this paper are not publicly available at this time but may be obtained from the corresponding author upon reasonable request.

REFERENCES

1. I. Walmsley, “Quantum optics: science and technology in a new light,” *Science* **348**, 525–530 (2015).
2. F. Flamini, N. Spagnolo, and F. Sciarrino, “Photonic quantum information processing: a review,” *Rep. Prog. Phys.* **82**, 016001 (2018).
3. A. Aspect, P. Grangier, and G. Roger, “Experimental tests of realistic local theories via Bell’s theorem,” *Phys. Rev. Lett.* **47**, 460–463 (1981).
4. P. W. Shor, “Polynomial-time algorithms for prime factorization and discrete logarithms on a quantum computer,” *SIAM Rev.* **26**, 1484–1509 (1997).
5. A. K. Ekert, “Quantum cryptography based on Bell’s theorem,” *Phys. Rev. Lett.* **67**, 661–663 (1991).
6. D. Bouwmeester, J.-W. Pan, K. Mattle, M. Eibl, H. Weinfurter, and A. Zeilinger, “Experimental quantum teleportation,” *Nature* **390**, 575–579 (1997).
7. P. G. Kwiat, K. Mattle, H. Weinfurter, A. Zeilinger, A. V. Sergienko, and Y. Shih, “New high-intensity source of polarization-entangled photon pairs,” *Phys. Rev. Lett.* **75**, 4337–4341 (1995).
8. P. G. Kwiat, E. Waks, A. G. White, I. Appelbaum, and P. H. Eberhard, “Ultrabright source of polarization-entangled photons,” *Phys. Rev. A* **60**, R773–R776 (1999).
9. B.-S. Shi and A. Tomita, “Generation of a pulsed polarization entangled photon pair using a Sagnac interferometer,” *Phys. Rev. A* **69**, 013803 (2004).
10. T. Kim, M. Fiorentino, and F. N. C. Wong, “Phase-stable source of polarization-entangled photons using a polarization Sagnac interferometer,” *Phys. Rev. A* **73**, 012316 (2006).
11. A. Dousse, J. Suffczynski, A. Beveratos, O. Krebs, A. Lemaître, I. Sagnes, J. Bloch, P. Voisin, and P. Senellart, “Ultrabright source of entangled photon pairs,” *Nature* **466**, 217–220 (2010).
12. M. Müller, S. Bounouar, K. D. Jöns, M. Glässl, and P. Michler, “On-demand generation of indistinguishable polarization-entangled photon pairs,” *Nat. Photonics* **8**, 224–228 (2014).
13. D. Huber, M. Reindl, Y. Huo, H. Huang, J. S. Wildmann, O. G. Schmidt, A. Rastelli, and R. Trotta, “Highly indistinguishable and strongly entangled photons from symmetric GaAs quantum dots,” *Nat. Commun.* **8**, 15506 (2017).
14. K. D. Jöns, L. Schweickert, M. A. Versteegh, D. Dalacu, P. J. Poole, A. Gulinatti, A. Giudice, V. Zwiller, and M. E. Reimer, “Bright nanoscale source of deterministic entangled photon pairs violating Bell’s inequality,” *Sci. Rep.* **7**, 1700 (2017).
15. J. Liu, R. Su, Y. Wei, B. Yao, S. F. C. da Silva, Y. Yu, J. Iles-Smith, K. Srinivasan, A. Rastelli, J. Li, and X. Wang, “A solid-state source of strongly entangled photon pairs with high brightness and indistinguishability,” *Nat. Nanotechnol.* **14**, 586–593 (2019).
16. N. Matsuda, H. Le Jeannic, H. Fukuda, T. Tsuchizawa, W. J. Munro, K. Shimizu, K. Yamada, Y. Tokura, and H. Takesue, “A monolithically integrated polarization entangled photon pair source on a silicon chip,” *Sci. Rep.* **2**, 817 (2012).

17. A. Vallés, M. Hendrych, J. Svozilik, R. Machulka, P. Abolghasem, D. Kang, B. Bijlani, A. Helmy, and J. Torres, "Generation of polarization-entangled photon pairs in a Bragg reflection waveguide," *Opt. Express* **21**, 10841–10849 (2013).
18. R. T. Horn, P. Kolenderski, D. Kang, P. Abolghasem, C. Scarcella, A. Della Frera, A. Tosi, L. G. Helt, S. V. Zhukovsky, J. E. Sipe, G. Weihs, A. S. Helmy, and T. Jennewein, "Inherent polarization entanglement generated from a monolithic semiconductor chip," *Sci. Rep.* **3**, 2314 (2013).
19. A. Orioux, A. Eckstein, A. Lemaître, P. Filloux, I. Favero, G. Leo, T. Coudreau, A. Keller, P. Milman, and S. Ducci, "Direct Bell states generation on a III-V semiconductor chip at room temperature," *Phys. Rev. Lett.* **110**, 160502 (2013).
20. L. Sansoni, K. H. Luo, C. Eigner, R. Ricken, V. Quiring, H. Herrmann, and C. Silberhorn, "A two-channel, spectrally degenerate polarization entangled source on chip," *npj Quantum Inf.* **3**, 5 (2017).
21. J. M. Donohue, M. Mastrovich, and K. J. Resch, "Spectrally engineering photonic entanglement with a time lens," *Phys. Rev. Lett.* **117**, 243602 (2016).
22. V. Ansari, J. M. Donohue, B. Brecht, and C. Silberhorn, "Tailoring non-linear processes for quantum optics with pulsed temporal-mode encodings," *Optica* **5**, 534–550 (2018).
23. J.-P. W. MacLean, J. M. Donohue, and K. J. Resch, "Direct characterization of ultrafast energy-time entangled photon pairs," *Phys. Rev. Lett.* **120**, 053601 (2018).
24. L. Olislager, J. Cussey, A. T. Nguyen, P. Emplit, S. Massar, J.-M. Merolla, and K. P. Huy, "Frequency-bin entangled photons," *Phys. Rev. A* **82**, 013804 (2010).
25. M. Kues, C. Reimer, J. M. Lukens, W. J. Munro, A. M. Weiner, D. J. Moss, and R. Morandotti, "Quantum optical microcombs," *Nat. Photonics* **13**, 170–179 (2019).
26. Y. Chen, M. Fink, F. Steinlechner, J. P. Torres, and R. Ursin, "Hong-Ou-Mandel interferometry on a biphoton beat note," *npj Quantum Inf.* **11**, 43 (2019).
27. S. Olmschenk, D. Matsukevich, P. Maunz, D. Hayes, L.-M. Duan, and C. Monroe, "Quantum teleportation between distant matter qubits," *Science* **323**, 486–489 (2009).
28. Z. Y. Ou and L. Mandel, "Observation of spatial quantum beating with separated photodetectors," *Phys. Rev. Lett.* **61**, 54–57 (1988).
29. J. G. Rarity and P. R. Tapster, "Two-color photons and nonlocality in fourth-order interference," *Phys. Rev. A* **41**, 5139–5146 (1990).
30. F. Kaneda, H. Suzuki, R. Shimizu, and K. Edamatsu, "Direct generation of frequency-bin entangled photons via two-period quasi-phase-matched parametric downconversion," *Opt. Express* **27**, 1416–1424 (2019).
31. X. Li, L. Yang, X. Ma, L. Cui, Z. Y. Ou, and D. Yu, "All-fiber source of frequency-entangled photon pairs," *Phys. Rev. A* **79**, 033817 (2009).
32. R.-B. Jin, R. Shiina, and R. Shimizu, "Quantum manipulation of biphoton spectral distributions in a 2D frequency space," *Opt. Express* **26**, 21153–21158 (2018).
33. S. Ramelow, L. Ratschbacher, A. Fedrizzi, N. K. Langford, and A. Zeilinger, "Discrete tunable color entanglement," *Phys. Rev. Lett.* **103**, 253601 (2009).
34. J. W. Silverstone, D. Bonneau, K. Ohira, N. Suzuki, H. Yoshida, N. Iizuka, M. Ezaki, C. M. Natarajan, M. G. Tanner, R. H. Hadfield, V. Zwiller, G. D. Marshall, J. G. Rarity, J. L. O'Brien, and M. G. Thompson, "On-chip quantum interference between silicon photon-pair sources," *Nat. Photonics* **8**, 104–108 (2014).
35. X. Caillet, V. Berger, G. Leo, and S. Ducci, "A semiconductor source of counterpropagating twin photons: a versatile device allowing the control of the two-photon state," *J. Mod. Opt.* **56**, 232–239 (2009).
36. A. Orioux, X. Caillet, A. Lemaître, P. Filloux, I. Favero, G. Leo, and S. Ducci, "Efficient parametric generation of counterpropagating two-photon states," *J. Opt. Soc. Am. B* **28**, 45–51 (2011).
37. A. De Rossi and V. Berger, "Counterpropagating twin photons by parametric fluorescence," *Phys. Rev. Lett.* **88**, 043901 (2002).
38. Y.-H. Kim, S. P. Kulik, M. V. Chekhova, W. P. Grice, and Y. Shih, "Experimental entanglement concentration and universal Bell-state synthesizer," *Phys. Rev. A* **67**, 010301 (2003).
39. G. Boucher, T. Douce, D. Bresteau, S. P. Walborn, A. Keller, T. Coudreau, S. Ducci, and P. Milman, "Toolbox for continuous-variable entanglement production and measurement using spontaneous parametric down-conversion," *Phys. Rev. A* **92**, 023804 (2015).
40. M. Barbieri, E. Roccia, L. Mancino, M. Sbroscia, I. Gianani, and F. Sciarrino, "What Hong-Ou-Mandel interference says on two-photon frequency entanglement," *Sci. Rep.* **7**, 7247 (2017).
41. T. Douce, A. Eckstein, S. P. Walborn, A. Z. Khoury, S. Ducci, A. Keller, T. Coudreau, and P. Milman, "Direct measurement of the biphoton Wigner function through two-photon interference," *Sci. Rep.* **3**, 3530 (2013).
42. A. Eckstein, G. Boucher, A. Lemaître, P. Filloux, I. Favero, G. Leo, J. E. Sipe, M. Liscidini, and S. Ducci, "High-resolution spectral characterization of two photon states via classical measurements," *Laser Photon. Rev.* **8**, L76–L80 (2014).
43. M. Halder, S. Tanzilli, H. de Riedmatten, A. Beveratos, H. Zbinden, and N. Gisin, "Photon-bunching measurement after two 25-km-long optical fibers," *Phys. Rev. A* **71**, 042335 (2005).
44. S. Tanzilli, W. Tittel, H. De Riedmatten, H. Zbinden, P. Baldi, M. DeMicheli, D. B. Ostrowsky, and N. Gisin, "PPLN waveguide for quantum communication," *Eur. Phys. J. D* **18**, 155–160 (2002).
45. J. Wang, A. Santamato, P. Jiang, D. Bonneau, E. Engin, J. W. Silverstone, M. Lerner, J. Beetz, M. Kamp, S. Höfling, M. G. Tanner, C. M. Natarajan, R. H. Hadfield, S. N. Dorenbos, V. Zwiller, J. L. O'Brien, and M. G. Thompson, "Gallium arsenide quantum photonic waveguide circuits," *Opt. Commun.* **327**, 49–55 (2014).
46. J. Belhassen, F. Baboux, Q. Yao, M. Amanti, I. Favero, A. Lemaître, W. Kolthammer, I. Walmsley, and S. Ducci, "On-chip III-V monolithic integration of heralded single photon sources and beamsplitters," *Appl. Phys. Lett.* **112**, 071105 (2018).
47. C. P. Dietrich, A. Fiore, M. G. Thompson, M. Kamp, and S. Höfling, "GaAs integrated quantum photonics: towards compact and multifunctional quantum photonic integrated circuits," *Laser Photon. Rev.* **10**, 870–894 (2016).
48. F. Boitier, A. Orioux, C. Autebert, A. Lemaître, E. Galopin, C. Manquest, C. Sirtori, I. Favero, G. Leo, and S. Ducci, "Electrically injected photon-pair source at room temperature," *Phys. Rev. Lett.* **112**, 183901 (2014).
49. S. Gronenborn, J. Pollmann-Retsch, P. Pekarski, M. Miller, M. Strösser, J. Kolb, H. Mönch, and P. Loosen, "High-power VCSELS with a rectangular aperture," *Appl. Phys. B* **105**, 783–792 (2011).
50. S. Francesconi, F. Baboux, A. Raymond, N. Fabre, G. Boucher, A. Lemaître, P. Milman, M. I. Amanti, and S. Ducci, "Engineering two-photon wavefunction and exchange statistics in a semiconductor chip," *Optica* **7**, 316–322 (2020).
51. S. Francesconi, A. Raymond, N. Fabre, A. Lemaître, M. I. Amanti, P. Milman, F. Baboux, and S. Ducci, "Anyonic two-photon statistics with a semiconductor chip," *ACS Photon.* **8**, 2764–2769 (2021).
52. A. Lyons, G. C. Knee, E. Bolduc, T. Roger, J. Leach, E. M. Gauger, and D. Faccio, "Attosecond-resolution Hong-Ou-Mandel interferometry," *Sci. Adv.* **4**, eaap9416 (2018).
53. P. G. Kwiat, "Hyper-entangled states," *J. Mod. Opt.* **44**, 2173–2184 (1997).
54. Z. Xie, T. Zhong, S. Shrestha, X. Xu, J. Liang, Y.-X. Gong, J. C. Bienfang, A. Restelli, J. H. Shapiro, F. N. Wong, and C. W. Wong, "Harnessing high-dimensional hyperentanglement through a biphoton frequency comb," *Nat. Photonics* **9**, 536–542 (2015).
55. F.-G. Deng, B.-C. Ren, and X.-H. Li, "Quantum hyperentanglement and its applications in quantum information processing," *Sci. Bull.* **62**, 46–68 (2017).
56. F. Steinlechner, S. Ecker, M. Fink, B. Liu, J. Bavaresco, M. Huber, T. Scheidl, and R. Ursin, "Distribution of high-dimensional entanglement via an intra-city free-space link," *Nat. Commun.* **8**, 15971 (2017).
57. P. Vergeyris, F. Mazeas, E. Gouzien, L. Labonté, O. Alibart, S. Tanzilli, and F. Kaiser, "Fibre based hyperentanglement generation for dense wavelength division multiplexing," *Quantum Sci. Technol.* **4**, 045007 (2019).
58. S. Ecker, F. Bouchard, L. Bulla, F. Brandt, O. Kohout, F. Steinlechner, R. Fickler, M. Malik, Y. Guryanova, R. Ursin, and M. Huber, "Overcoming noise in entanglement distribution," *Phys. Rev. X* **9**, 041042 (2019).
59. J.-H. Kim, Y. Kim, D.-G. Im, C.-H. Lee, J.-W. Chae, G. Scarcelli, and Y.-H. Kim, "Noise-resistant quantum communications using hyperentanglement," *Optica* **8**, 1524–1531 (2021).
60. Z.-Y. J. Ou, *Multi-Photon Quantum Interference* (Springer US, 2007).